AISTech 2023 — Proceedings of the Iron & Steel Technology Conference
8–11 May 2023, Detroit, Mich., USA
DOI: 10.33313/387/042

Investigation of the Thermally Thick Alternative Reducing Agent Behavior in the Raceway Zone

Matthias Kiss[1], Markus Bösenhofer[1,2], Franz Hauzenberger[3], Hugo Stocker[4], Christoph Feilmayr[5], Michael Harasek[1]

[1]K1-Met GmbH, Area 4 – Simulation and Analyses
Stahlstrasse 14, BG 88, Linz, Austria 4020
Phone: +43 1 58801 166232
Email: matthias.kiss@k1-met.com

[2]TU Wien, Institute of Chemical, Environmental and Bioscience Engineering
Getreidemarkt 9/166, Vienna, Austria, 1060

[3]Primetals Technologies Austria GmbH
Turmstraße 44, Linz, Austria, 4031

[4]voestalpine Stahl Donawitz GmbH
Kerpelystraße 199, Leoben, Austria, 8700

[5]voestalpine Stahl GmbH
voestalpine-Straße 3, Postfach 3, Linz, Austria 4020

ABSTRACT

Alternative reducing agents (ARAs) injected into the raceway zone of the blast furnace have diameters in the range of tens to thousands of micrometers. Larger ARA particles can develop significant internal temperature and species concentration gradients. These gradients determine the thermochemical ARA conversion characteristics. To capture these effects, a resolved Lagrangian particle model was developed, which solves mass and energy transport equations on a 1D grid. The influence of the resolved model on the conversion characteristics in the raceway zone is compared to classical unresolved or 0D Lagrangian models using computational fluid dynamics simulations in OpenFOAM®.

Keywords: Blast furnace, PCI, CFD, Lagrangian particle model, resolved particle model, OpenFOAM®

INTRODUCTION

Pulverized Coal Injection (PCI) is a method commonly used to decrease coke consumption and increase productivity in blast furnaces.[1] An ecologically attractive alternative for using pulverized coal in the raceway zone of the blast furnace is to use biomass, or plastic pellets as alternative reducing agents (ARAs). While the PCI particles commonly have diameters in the range of 10s to 100s of micrometers other ARAs can have sizes in the range of millimeters.[1] A common approach to numerically model PCI in the raceway zone is to use Euler-Lagrange computational fluid dynamics (CFD) models. These discrete Lagrangian particles interact and exchange mass and energy with the continuous fluid phase. The currently implemented Lagrangian models in OpenFOAM assume 0D particles and only estimate particle surface values but neglect temperature and species gradients inside the particle.[2] For small particles these gradients are assumed to be negligible, but they can be influential in larger, thermally thick particles such as plastic pellets and biomass.[3] Therefore, we present a Lagrangian particle model for thermally thick reducing agents in OpenFOAM. The model resolves internal gradients by extending the commonly used 0D point model to a 1D model with internal grid-points. In the following, we will first introduce the theory behind this novel Lagrangian particle model and then compare the 1D model to a classical 0D model to evaluate the influence of the thermally thick behavior in the raceway zone on the particle conversion.

MODELING THEORY

The carrier phase coupling is similar for the 0D and thermally thick (1D) model and uses the same interface for mass and energy exchange between particle and carrier phase. Therefore, existing 0D models can easily be swapped for the 1D model in OpenFOAM without the need to adjust the Eulerian part of the simulation. However, inside the 1D model the calculations differ from the 0D model. In the following, the relevant aspects of the 1D model will be described, while the reader is referred to the existing literature about the 0D model [4]

Inside the 1D model a set of transport equations is solved for temperature and species concentrations and connected to the carrier phase via a set of boundary conditions (BCs). In the 0D model only surface values are interpolated from the carrier phase onto the particle and used to calculate chemical conversion rates and particle heat-up. The 1D model is internally resolved by using several grid-points inside the particle. The idea behind that is to reduce a 3D particle to homogeneous, concentric layers that are each represented by a single grid-point. Simple particle shapes like spheres, cylinders, or slabs, can be chosen by introducing the geometric relation Γ, which influences the layer volumes and the exchange terms between neighboring layers.[5] In this study we will focus on spherical particles and the term Γ has the following form:

$$\Gamma = \frac{4}{3}\pi({r_i}^3 - {r_{i-1}}^3) \tag{1}$$

where r_i is the radius of the layer *i* and r_{i-1} is the radius of the previous layer**.** The factor Γ is used when calculating the transport equations inside the particle to achieve correct transport terms between layers considering the shape of the particle (see Equations 2 and 3). The 1D model is a multiphase model that contains three separate phases: gas, liquid and solid. Each of the phases has a mass fraction with regards to the total layer mass and mass fractions for each species within a phase. Further each of the phases is assigned separate values for heat capacity, thermal conductivity, and density. The solid and liquid phases are assumed to be stationary, while transport equations for diffusion are solved for the gas phase with a convective BC that couples it to the carrier phase. That means that mass can only be transferred between particle and carrier phase via the gas phase. The mass transport equation for the gas phase looks as follows:

$$\frac{dY_i}{dt} = \frac{1}{\Gamma(r)}\frac{d}{dr}\left(D\Gamma(r)\frac{dY_i}{dr}\right) + S_{Yi} \tag{2}$$

where Y_i is the molar concentration of species *i* inside a layer, *D* is the diffusion coefficient, and S_{Yi} is an explicit source term supplied by the chemistry sub-model. The diffusion coefficient is fitted as a polynomial of second degree using kinetic gas theory data from Cantera for a O2-N2 binary mixture.[6] The temperature equation is solved using effective values for the heat capacity and thermal conductivity that are calculated using all three phases. The effective heat-transfer equation has the form:

$$\frac{dT}{dt} = \frac{1}{\Gamma(r)}\frac{d}{dr}\left(\kappa\Gamma(r)\frac{dT}{dr}\right) + S_T \tag{3}$$

with *T* being the temperature of each layer, κ being the thermal conductivity, and S_T being the explicit source due to chemical reactions. The mass transport equation is coupled with the carrier phase via the following advective BC:

$$D\frac{dY_i}{dr}|_{r=R} = -mtc \cdot (Y_{iC} - Y_i) \tag{4}$$

where *mtc* is the mass transport coefficient calculated using the Frossling correlation.[7] Y_{iC} is the molar concentration of species *i* in the carrier phase interpolated to the particle location within the containing cell, and *R* is the outer particle radius. The heat-transfer equation uses advective and radiative BCs:

$$\kappa\frac{dT}{dr}|_{r=R} = -htc \cdot (T_C - T) - \epsilon \cdot (T_C^4 - T^4) \tag{5}$$

where *htc* is the heat transfer coefficient calculated according to the Ranz-Marshall correlation.[8]**.** T_C is the carrier phase temperature interpolated to the particle surface and *ε* is the emission coefficient. The transport equations (Equations 2 and 3) combined with their BCs (Equations 4 and 5) are discretized for each grid-point using second order schemes for the derivatives in space and integrated over time using an implicit Euler scheme, which leads to mass and energy conservation and allows for numerical stability even with large time-steps and a small number of grid-points. The matrix equation given by the implicit algorithm is solved using the LU-decomposition method implemented in OpenFOAM.

Inside each layer of the particle a chemistry model is solved using the species concentrations and temperatures assigned to each of the layers. The chemistry model is comprised of four independent sub-models: drying, pyrolysis, oxidation and gasification. The drying model employs the thermal approach by Haberle, Haugen, and Skreiberg [9],where the heat flux into each layer is calculated, multiplied with an effectiveness factor and then used to calculate the amount of liquid water that can be evaporated with the energy supplied by the heat flux at the given layer temperature and carrier-phase-pressure. The evaporated mass is then subtracted from the liquid phase and added to the gas-phase as water vapor, which can diffuse out of the particle. The pyrolysis, oxidation, and gasification models use an Arrhenius approach to determine reaction rates r_k.

$$r_k = A \cdot exp\left(-\frac{E_a}{RT}\right) \tag{6}$$

where A is the pre-exponential factor, E_a is the activation energy and R is the specific gas constant. Each layer can be comprised of several different solid species that all can be pyrolyzed independently. The pyrolysis products can be a combination of solid and gas phase species. The oxidation and gasification models employ heterogeneous reactions that have solid and gas phase species educts and only gas phase species as products.

A list of all the reactions used inside the particle and the carrier gas and their parameters can be found in Table 1 and Table 2, respectively. To calculate the surface reaction rates the 0D model uses only the outer particle surface. The 1D model considers the porosity corrected outer surface and the inner pore surface as reactive surface. Then it uses the inner specific surface to calculate the reactive surface inside the particle pores. The 1D model then solves transport equations for all gas phase species and uses the resulting concentrations in each layer to calculate surface reaction rates using the specific inner surface as well as the outer surface. The 0D model uses the empirical two-third rule to calculate the concentration of gas phase species at the particle surface and then uses this value and the outer particle surface to calculate the reaction rates.[4]

Table 1. Heterogeneous Reactions Inside 1D Model Units in kmol, m^2, K, s, J [10]

	Reaction	**A**	**E_a**
R1	$C + 0.5O_2 \rightarrow CO$	0.8598	$1.494 \cdot 10^8$
R2	$C + CO_2 \rightarrow 2CO$	0.02438	$1.751 \cdot 10^8$
R3	$C + H_2O \rightarrow CO + H_2$	0.02438	$1.751 \cdot 10^8$
R4	$C + 2H_2 \rightarrow CH_4$	$1.1846 \cdot 10^{-6}$	$1.490 \cdot 10^8$

Table 2. Gas Phase Reactions in Carrier Phase, Units of kmol, m^2, K, s, J (R5-R7 from [11], R8+R9 from [12])

	Reaction	**A**	**E_a/R**
R5	$CH_4 + 1.5O_2 \rightarrow CO + 2H_2O$	$5.03 \cdot 10^{11}$	24053
R6	CO + 0.5O2 → CO2	$2.24 \cdot 10^{12}$	20129
R7	CO2 → CO + 0.5 O2	$5 \cdot 10^8$	20481
R8	CO + H2O → CO2 + H2	$2.75 \cdot 10^9$	10064
R9	CO2 + H2 → CO + H2O	$9.98 \cdot 10^{10}$	14493

The 1D model also employs a shrinking model. The layer diameters are updated in each time-step by calculating the volume change due to the conversion of solid mass with known density. In most cases the solid mass conversion rates are different in each layer, which leads to non-uniform layer thicknesses. In this case the initially non-uniform grid is further adjusted to become equidistant again. The shift of energy, mass, and species compositions between the layers before and after the adjustment is compensated by calculating the corresponding exchange terms.

SIMULATION SETUP

OpenFOAM is used as the CFD framework for the simulations of the 1D and the 0D particle models. Due to the native implementation of the 1D model in OpenFOAM it is possible to set up the two identical simulations and only exchange the particle models, while the carrier phase is simulated using the compressible, multi-component solver reactingFoam with the k-ε turbulence model.

The number of grid-points inside the 1D model can be freely chosen at the beginning of each simulation (minimum of 2 points) and was set to 10 for this study. Ten grid points have in our experience been enough to satisfactorily resolve gradients, while also minimizing the computational cost of the model, as the LU-Decomposition employed to solve the Matrix equation scales like $O(2/3N^3)$ with the number of grid-points N. In each simulation a single particle is at a fixed position at the center of a cell. Lagrangian particles should not interfere with the flow field of the surrounding cells and therefore, we chose a cell size of 10x10x10 particle diameters [13]. This means that, while the number of cells and their geometry stays identical independently of particle diameters, the size of each cell and the size of the total simulation domain changes. The simulation domain is a simple cuboid with a total of 30 cells in x-direction and 15 cells each in y- and z-direction. The particle is centered in the y-z plane and at one quarter of the domain length in x-direction, which allows for an undisturbed flow field towards the boundaries of the simulation domain.

Table 3. Boundary Conditions (BCs) for the Simulation

Field	**Inlet-BCs**		**Wall-BCs**		**Outlet-BCs**	
	type	value	type	value	type	value
T	fixedValue	tabulated (Figure 1)	fixedValue	tabulated (Figure 1)	zeroGradient	-
U	fixedValue	tabulated (Figure 1)	fixedValue	tabulated (Figure 1)	zeroGradient	-
radiation	MarshakRadiation	-	MarshakRadiation	-	MarshakRadiation	-
K	turbulentIntensityKineticEnergyInlet	0.05	kqRWallFunction	-	inletOutlet	0.05
Epsilon	turbulentMixing-LengthDissipation-RateInlet	0.000525	epsilonWall-Function	-	zeroGradient	
P	zeroGradient	-	zeroGradient	-	fixedValue	$5 \cdot 10^5$ Pa
O2	fixedValue	0.30157	zeroGradient	-	zeroGradient	-
N2	fixedValue	0.6946	zeroGradient	-	zeroGradient	-
H2O	fixedValue	0.00383	zeroGradient	-	zeroGradient	-
Ydefault	fixedValue	0.0	zeroGradient	-	zeroGradient	-

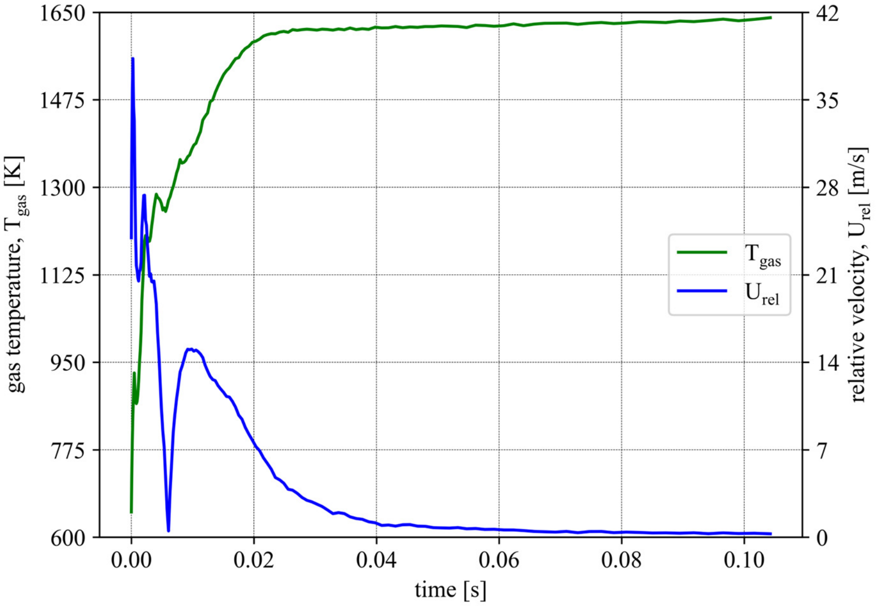

Figure 1. Values for gas temperature and velocity at simulation domain inlet. The shown velocities were set as the x-component of the velocity vector at the inlet.

The BCs are modeled according to the data from Bösenhofer et al [14] and represent the particle's trajectory through the raceway zone of a blast furnace form the particle's frame of reference. The BC values for temperature and velocity are shown in Figure 1. The data for relative velocity magnitude was set as the x-component of the velocity vector at the inlet and walls, while y, and z components were set to zero. This is valid due to the spherical particle's rotationally invariant frame of reference. The BCs for the other relevant fields are listed in Table 3. We investigate dry-char conversion in this study. The pyrolysis and drying models are implemented in a completely different manner in both models, while oxidation and gasification models are implemented very similarly. By excluding drying and pyrolysis we reduce the complexity of the particle conversion process and enable a more representative comparison between the two models. The relevant properties are listed in Table 4.[15–17] Furthermore, the global Westbrook-Dryer mechanism is employed in the carrier phase, which includes the water-gas-shift reactions.[11, 12] All reactions (particle and carrier phase) and their respective Arrhenius parameters are listed in Table 1 and Table 2.

Table 4. Parameters for the Modeled Char Particle

Name	**Value**	**Unit**
particle diameters	$5\cdot10^{-5}$, $1\cdot10^{-4}$, $5\cdot10^{-4}$, 0.001, 0.005, 0.01, 0.015	m
char density [15]	1450	kg/m^3
particle density [15]	880	kg/m^3
heat capacity [17]	2000	J/(kg K)
heat transfer coefficient [16]	1.33	$W/(m^2K)$
heating value char [15]	30	MJ/kg
porosity [15]	0.39	-
tortuosity [16]	5	-
internal surface [15]	15805	m^2/m^3

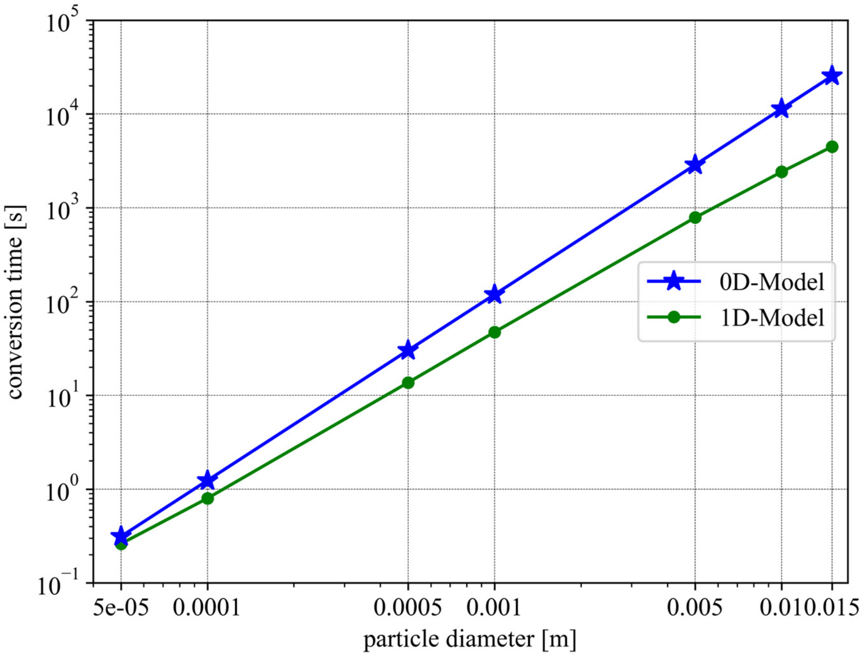

Figure 2. Time for 100% particle conversion vs. particle diameter. Double logarithmic plot, shows power law relation between conversion time and diameter.

Table 5. Conversion Times for Both Models

Diameter [m]	Conversion times [s]	
	1D Model	**0D Model**
$5 \cdot 10^{-5}$	0.2618	0.3131
0.0001	0.7984	1.2376
0.0005	13.6914	30.2014
0.001	47.2929	118.904
0.005	786.482	2868.36
0.01	2414.82	11360.3
0.015	4493.51	25458.1

RESULTS AND DISCUSSION

Similar char conversion simulations were performed with the 0D and 1D model using various particle diameters to assess thermal-thick behavior. Table 5 summarizes the used particle diameters and the overall conversion times. Figure 2 compares the conversion times for each model at different diameter. While both models' conversion times increase with growing diameters, the 1D model conversion is outpacing the 0D model. The exact conversion times are listed in Table 5. The conversion times follow a power law as can be seen by the points being approximately on straight lines in the log-log plot in Figure 2. This is expected due to the particle volume and surface relationship to the diameter of d^3 and d^2, respectively. Figure 3 shows the temperature evolution over time for the smallest particle size ($5 \cdot 10^{-5}$ m). Figure 3 (a) shows the whole burnout, while Figure 3 (b) is zoomed in on the heat-up phase.

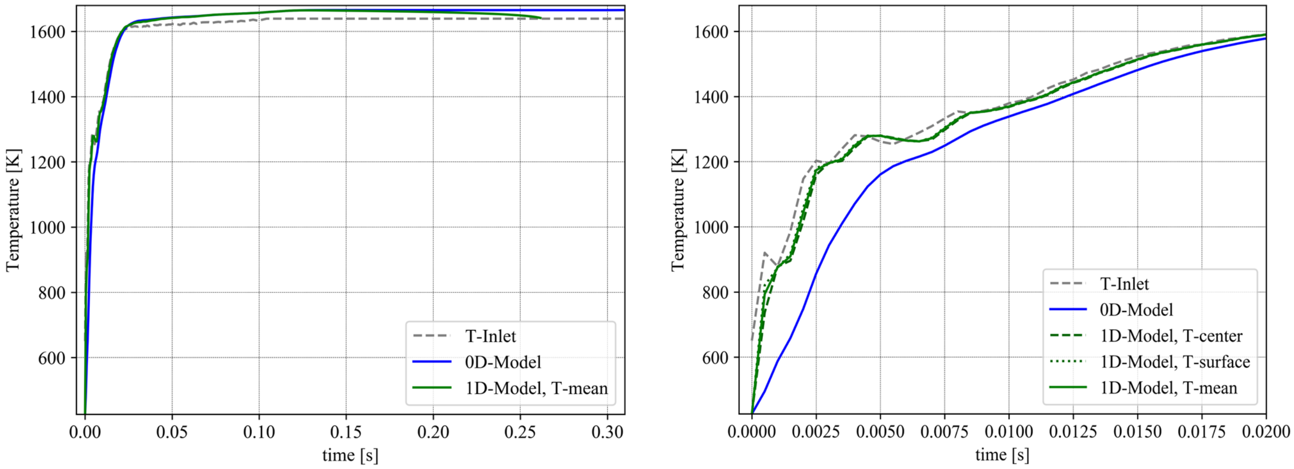

(a) (b)

Figure 3. Particle and inlet temperature for both models at particle diameter $5 \cdot 10^{-5}$ m. (a) Full temperature curve until 100% conversion. (b) Zoomed in heat-up period with additional center, surface, and mean temperatures for 1D model.

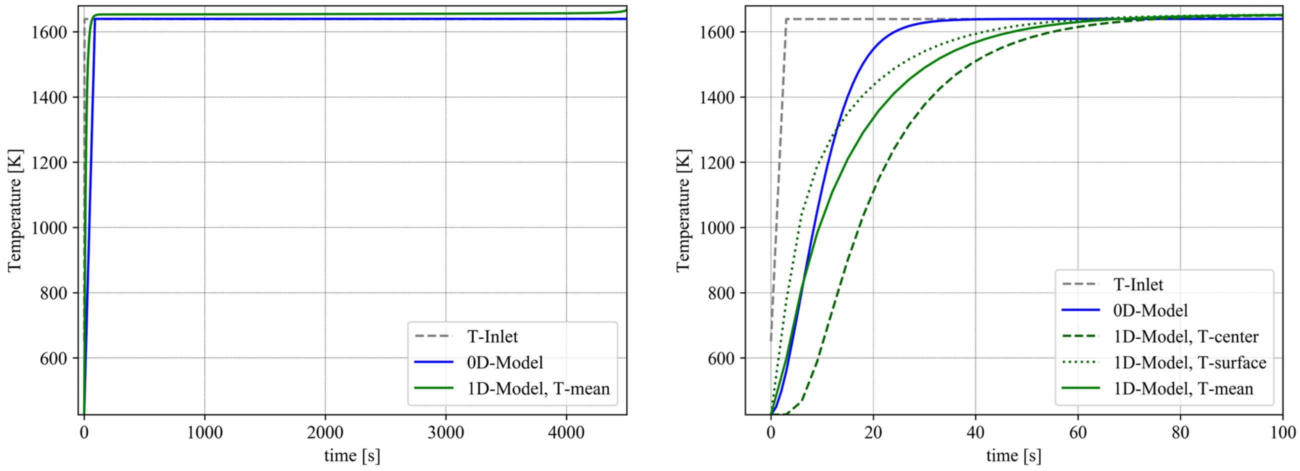

(a)

(b)

Figure 4. Particle temperatures and inlet temperature for both models at particle diameter 0.015 m. (a) Full temperature curve until 100% conversion. (b) Zoomed in heat-up period with additional center, surface, and mean temperatures for 1D model.

The 1D model increases in temperature faster than the 0D model during the heat-up in the beginning of the simulation but then converges at the same temperature as the 0D model, before cooling off to the carrier gas temperature close to burnout. For this particle size the internal temperature gradient during the heat-up phase is small as seen in Figure 3 (b), with less than 50 Kelvin (see also Figure 5). Figure 4 shows the same temperature profiles for the 15 mm particle as Figure 3 shows for the 50 µm particle. Figure 4 (a) is cut off at the burnout time of the 1D model as the 0D model temperature does not change until the burnout at 25458 s. Figure 4 (b) reveals that the 0D model heats up faster for the large particle, while also showing that considerable internal gradients develop during the heat-up phase when using the 1D model. The energy transport from the surface to the colder particle center leads to the slower heat-up of the 1D model.

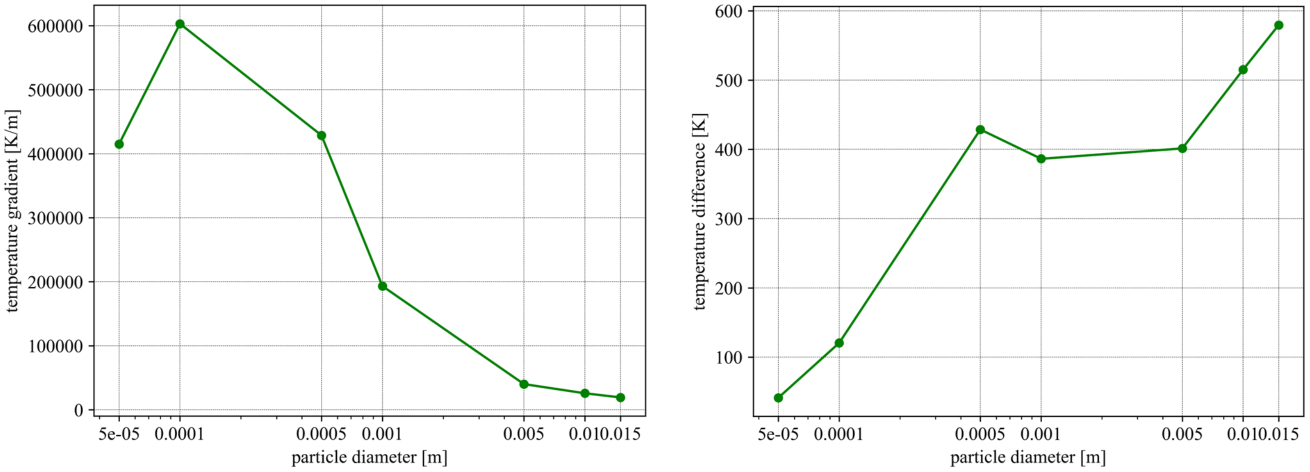

(a)

(b)

Figure 5. Temperature gradient (a) calculated as temperature difference between particle center and surface over the particle diameter (Equation 7) and temperature difference (b) between particle center and surface at the time at which the mean particle temperature reaches 1032 K.

Figure 5 (a) depicts the internal temperature gradient between particle center and surface for each particle size at the halfway point of the heat-up phase, at 1032 K. In Figure 5 (a) the temperature gradient is shown as,

$$\frac{dT}{dr} = \frac{\left(T_{surface} - T_{center}\right)}{d_p/2} \tag{7}$$

where d_p is the particle diameter. Figure 5 (b) shows the absolute values of the temperature difference between surface and center of the particle. The absolute temperature difference between the particle center and surface increase with increasing particle diameters. The particles with diameters 0.5 mm and 1 mm show a deviation from that trend. The reason is that the carrier temperature profile (see Figure 3) is not steady and has a few dips that happen around the point where the temperature data is taken for those simulations. These dips in gas-phase temperature influence the particle surface temperature and can lead to a departure from the expected heat-up behavior. The temperature gradient of Figure 5 (a) shows the inverse behavior, where the particle size is leading to smaller particles being the ones with higher gradients. The particle size changes by multiple orders of magnitude, while the temperature differences are ranging from 50 K to 600 K. The reason why the internal temperature gradients are higher in smaller particles is that the heating rates do not have a linear relationship with the particle diameter. While the smallest particle temperature converges at about 0.025 s (see Figure 3) it takes about 70 s for the largest particle (see Figure 4). That means that the largest particle, with 300 times the smallest particle's diameter, takes about 2800 times longer to reach temperature convergence. This is due to the heat-transfer into the particle scaling with the particle surface, while the temperature transport inside the particle is a function of the particle volume. Therefore, the larger particles heat up slower and develop smaller temperature gradients despite the absolute temperature difference between the particle center and surface being larger than for smaller particles.

Additionally, to the differences in heat-up and temperature gradients the two models employ a different approach to calculating mass conversion rates. The 1D model uses the outer particle surface weighted with the particle porosity in the outermost layer, as well as a specific inner surface to calculate conversion rates inside each layer. These conversion rates further depend on the gas phase concentrations in each layer resulting from Equations 2 and 4. The 0D model only uses the outer particle surface and the 2/3 rule that uses the carrier phase gas concentrations to approximate for the gas concentrations at the particle surface.[4] The 1D model however allows for the calculation of gas phase concentrations in each layer of the particle. In Figure 6 the mass conversion rates are shown for the smallest diameter (50 µm) for both models. It can be seen that in the 1D model the outermost layer is responsible for the main part of the total particle mass loss.

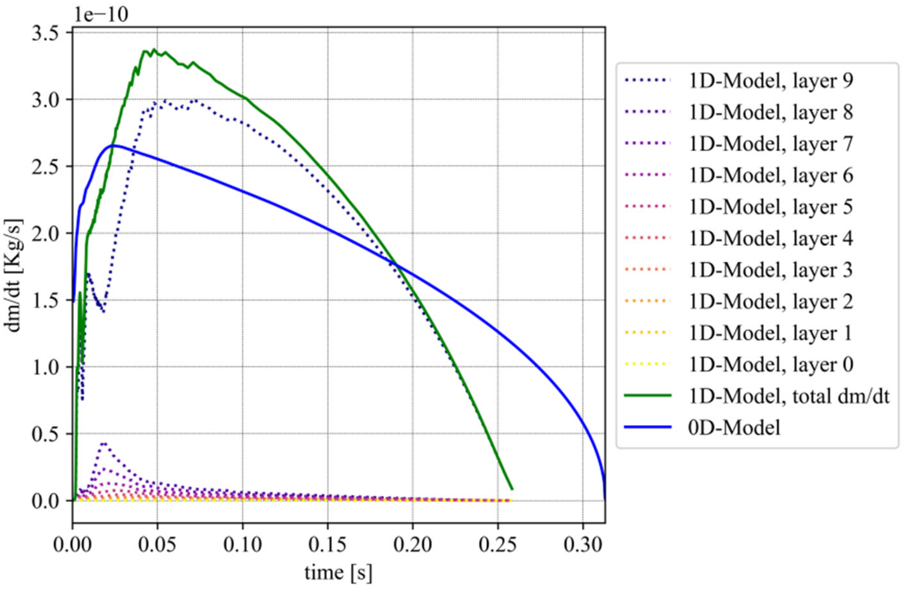

Figure 6. Mass conversion rates for the $5 \cdot 10^{-5}$ m particle. Total conversion rates are shown for both models (solid lines), as well as conversion contributions per layer for the 1D model.

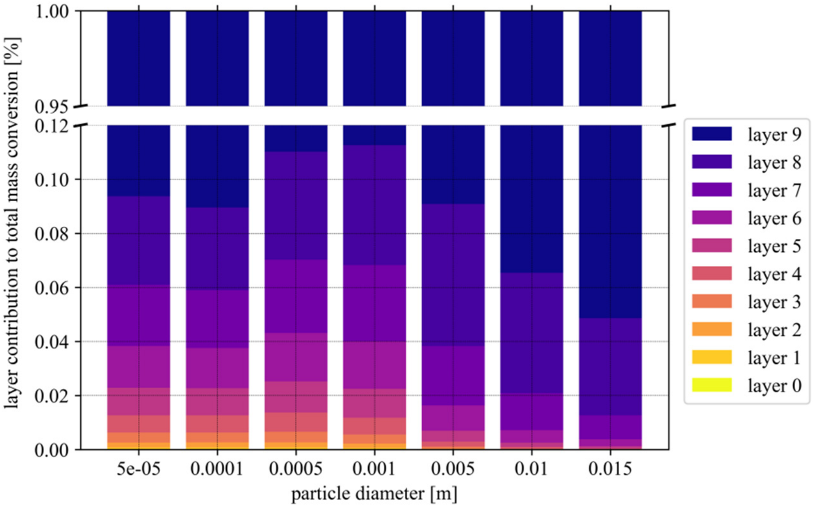

Figure 7. The percentage each layer contributes to the total mass loss over the whole conversion process for each particle diameter. The y-axis is cut for better visibility of the inner layer contributions.

Figure 7 shows the percentage of the total mass conversion of the 1D model that each layer contributes, integrated over the whole conversion process. It is visible that the outermost layer is the dominant layer consistently for all diameters with 89% to 95% of the total mass conversion happening there. This tendency increases towards larger diameters. Figure 8 shows the initial surface for the 1D model divided by the outer particle surface (equal to the 0D model reactive surface). The 1D model surface is the internal surface of each layer with the porosity adjusted outer particle surface added to the outermost layer. While the total available reactive surface in the 1D model is smaller than in the 0D model for the first two diameters it quickly outpaces the 0D model due to the internal surface contributions. At the same time, the available reactive surface is more evenly distributed between layers for larger diameters, which shows that the inner surface outgrows the outer particle surface in the 1D model with increasing diameter.

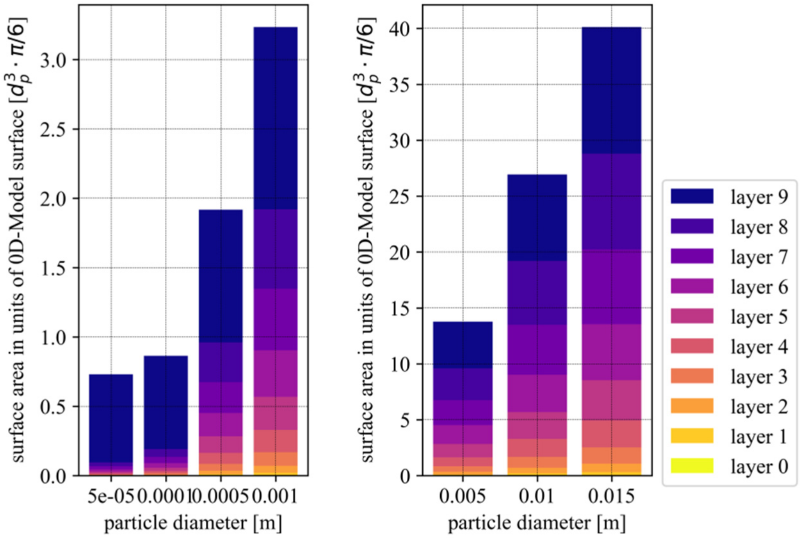

(a) (b)

Figure 8. Shown is the available reactive surface in each layer of the 1D model in units of the 0D model reactive surface (equal to the outer particle surface). (a) Shows the first 4 particle diameters, while (b) shows the largest 3 diameters. The plot is split into two subplots for easier readability.

Further the more sophisticated mass transport model (Equation 2) of the 1D model with the convective BC (Equation 4) allows to better estimate the O_2 concentrations at the particle surface as well as to calculate how far O_2 can penetrate the resolved particle, resulting in higher O_2 concentrations at the surface of the particle for the 1D model. However, as indicated by Figure 7, the conversion mainly occurs at the outermost layer of the model because most of the available oxygen is consumed there. In total this leads to the similar conversion times for small diameters where the 1D model has a smaller total reactive surface than the 0D model. For larger diameters, where the reactive surface of the 1D model's outermost layer alone is larger than the 0D model's reactive surface, this leads to even faster conversion times in the 1D model. Due to the conversion being mostly limited to the outermost particle layer in the 1D model the internal temperature gradients (Figure 5) are only of little influence on the conversion times and the main reason for the faster conversion times lies in the combination of higher O_2 concentrations as well as the larger accessible reactive surface of the 1D model.

CONCLUSIONS

The use of a 1D Lagrangian particle model has been shown to deliver different results than an unresolved 0D model for char conversion inside the raceway zone of a blast furnace. Inside the resolved particle, considerable temperature and species gradients were found which are not considered in the 0D model. The investigation of the internal gradients together with the inclusion of an internal reactive surface allows us to identify the following reasons as to why the 1D model shows significantly faster conversion times with increasing particle diameter than the 0D model:

- A slightly larger temperature at the particle surface due to a more sophisticated heat transport model that takes radiative and convective heat transfer at the particle surface, as well as the heat transfer into the particle itself, into account.
- The temperature gradients inside the particle have little direct consequence as the conversion happens mainly close to the particle surface.
- Higher oxygen concentrations at the surface and inside the 1D model due to the resolved mass transport model.
- Oxygen penetration into the particle being neglected in the 0D model, while the 1D model takes conversion at the inner particle surface into account.
- The inner particle surface scales with the particle volume, and therefore oxygen penetration into the outermost layer of the 1D model leads conversion rates that scale faster with increasing particle diameter.

These preliminary results hint on the importance of resolving internal gradients for the conversion of larger particles inside the raceway zone of the blast furnace. Further studies are needed to compare the 1D model with experimental data for validation of the results. Such a study that compares the 1D model to experimental data for the conversion of large biomass particles, including pyrolysis and drying, is currently already in progress and will be published soon. Preliminary results confirm the presented results.

ACKNOWLEDGMENTS

The authors gratefully acknowledge the funding support of K1-MET GmbH, Metallurgical Competence Center. The research program of the competence center K1-MET is supported by COMET (Competence Center for Excellent Technologies), the Austrian program for competence centers. COMET is funded by the Federal Ministry for Transport, Innovation and Technology, the Federal Ministry for Digital and Economic Affairs, the province of Upper Austria, Tyrol, and Styria.

Apart from funding, the project activities are financed by the industrial partners Primetals Technologies Austria, voestalpine Stahl and voestalpine Stahl Donawitz.

REFERENCES

1. H. Ahmed, "New trends in the application of carbon-bearing materials in blast furnace iron-making," *Minerals*, vol. 8, no. 12, pp. 1–20, 2018.
2. "OpenFoam.org." [Online]. Available: https://openfoam.org.
3. M. Bösenhofer, C. Jordan, and M. Harasek, "Radiative Heating of a Single Coal Particle Under Blast Furnace Conditions Radiative Heating of a Single Coal Particle Under Blast Furnace Conditions," in *14th Minisymposium Chemical and Process Engineering and 5th Austrian Particle Forum*, 2018, no. April.
4. M. Bösenhofer, "On the modeling of multi-phase reactive flows: Thermo-chemical conversion in the raceway zone of blast furnaces. Doctoral thesis," PhD Thesis, Technische Universität Wien, 2020.
5. H. Thunman, B. Leckner, F. Niklasson, and F. Johnsson, "Combustion of wood particles - A particle model for Eulerian calculations," *Combust Flame*, vol. 129, no. 1–2, pp. 30–46, 2002.
6. D. G. Goodwin, H. K. Moffat, I. Schoegl, R. L. Speth, and B. W. Weber, "Cantera: An Object-oriented Software Toolkit for Chemical Kinetics, Thermodynamics, and Transport Processes." 2022.

7. N. Frossling, “The evaporation of falling drops (in German),” *Gerlands Beiträge zur Geophysik*, no. 52, pp. 170–216, 1938.
8. W. Ranz and W. Marshall, “Evaporation from Drops,” *Chem Eng Prog*, vol. 48, no. 22, pp. 141–146, 1952.
9. I. Haberle, N. E. L. Haugen, and Ø. Skreiberg, “Drying of Thermally Thick Wood Particles: A Study of the Numerical Efficiency, Accuracy, and Stability of Common Drying Models,” *Energy & Fuels*, vol. 31, no. 12, pp. 13743–13760, Dec. 2017.
10. C. Y. Wen and T. Z. Chaung, “Entrainment Coal Gasification Modeling.,” *Coal Processing Technology*, vol. 5, no. 4, pp. 178–118, 1979.
11. C. K. Westbrook and F. L. Dryer, “Simplified Reaction Mechanisms for the Oxidation of Hydrocarbon Fuels in Flames,” *Combustion Science and Technology*, vol. 27, no. 1–2, pp. 31–43, 1981.
12. W. P. Jones and R. P. Lindstedt, “Global reaction schemes for hydrocarbon combustion,” *Combust Flame*, vol. 73, no. 3, pp. 233–249, 1988.
13. F. Evrard, F. Denner, and B. van Wachem, “Euler-Lagrange modelling of dilute particle-laden flows with arbitrary particle-size to mesh-spacing ratio,” *Journal of Computational Physics: X*, vol. 8, p. 100078, 2020.
14. M. Bösenhofer *et al.*, “Suitability of pulverised coal testing facilities for blast furnace applications,” *Ironmaking and Steelmaking*, vol. 47, no. 5, pp. 574–585, 2020.
15. P. A. Bejarano and Y. A. Levendis, “Single-coal-particle combustion in O2/N2 and O2/CO2 environments,” *Combust Flame*, vol. 153, no. 1–2, pp. 270–287, 2008.
16. C. R. Shaddix, F. Holzleithner, M. Geier, and B. S. Haynes, “Numerical assessment of Tognotti determination of CO2/CO production ratio during char oxidation,” *Combust Flame*, vol. 160, no. 9, pp. 1827–1834, 2013.
17. J. J. Murphy and C. R. Shaddix, “Combustion kinetics of coal chars in oxygen-enriched environments,” *Combust Flame*, vol. 144, no. 4, pp. 710–729, 2006.